DOI: 10.61782/fa.2025.0827

FORUM ACUSTICUM
EURONOISE 2025

STABILITY INVESTIGATIONS OF SOLID WALL IMMERSED BOUNDARY SCHEMES FOR THE LINEARIZED EULER EQUATIONS IN MULTIDIMENSIONS

Izsak, Marian G. S.[1*] **Kaltenbach, Hans-Jakob**[1]
[1] Flow Control and Aeroacoustics Group, School of Engineering and Design,
Technische Universität München, Boltzmannstraße 15, 85748 Garching, Germany

ABSTRACT

We investigate the numerical stability of our recently developed multidimensional sharp-interface immersed boundary treatment for equidistant Cartesian grids to solve the linearized Euler equations (LEE) for scattering problems and the linearized perturbed compressible equations (LPCE) for flow-induced aeroacoustic simulations in multidimensions. Instead of employing common ghost point techniques, we recently proposed designing modified finite-difference stencils for first derivatives near the solid wall that directly include the imposition of multiple boundary constraints, including a zero-vorticity constraint. We employ the matrix method, including the method-of-lines approach, to assess the numerical stability of our stencil design. We determine eigenvalues of the semi-discretized system of difference equations, including immersed obstacles, to identify the underlying parameters most contributing to the stability of our multidimensional boundary treatment. Conclusively, using a hybrid hydrodynamic/acoustic splitting approach, we simulate the classical aeolian sound produced by the low-Reynolds flow around a circular cylinder resolved by eight grid nodes per diameter in 2D via the LPCE without spatial filtering of the numerical solution.

Keywords: *stability analysis, immersed boundary, finite-difference method*

**Corresponding author*: marian.izsak@tum.de.
Copyright: *©2025 Marian G.S. Izsak et al. This is an open-access article distributed under the terms of the Creative Commons Attribution 3.0 Unported License, which permits unrestricted use, distribution, and reproduction in any medium, provided the original author and source are credited.*

1. INTRODUCTION

Since the pioneering work of Courant, Friedrichs, and Lewy (1928) on elliptic boundary and hyperbolic initial value problems [1], various techniques have emerged to assess the numerical stability of partial differential equation systems. Lax & Richtmyer [2] established that under certain conditions, stability ensures convergence.

Von Neumann's Fourier analysis [3] for finite difference equations on unbounded domains provided a practical stability framework by deriving eigenvalues from analytical dispersion relations. Vichnevetsky [4] further explored this approach. For bounded domains, Gustafsson, Kreiss & Sundström [5] (GKS theory) developed a general stability framework for finite difference approximations.

An alternative approach is the matrix method (Hirsch [6]), based on the method of lines [7–9], which examines the eigenvalues of spatially discretized problems using the Kreiss matrix theorem [10]. This method has been applied by Osher [11], Strikwerda [12], Sescu et al. [13], and Lele [14] to study finite-difference schemes for the linear advection equation.

Since the linear advection equation does not capture wave reflections at solid walls, the linearized Euler equations (LEE) must be studied for the stability analysis of boundary discretizations. Tam & Kurbatskii [15] analyzed the stability of their ghost-point-based immersed-boundary method for the LEE, improving stability through wavenumber-optimized extrapolation schemes in 1D. In our recent work [16], we adapted their method to prove the unconditional stability of a novel 1D immersed-boundary formulation, demonstrating that stability depends on the number of enforced boundary constraints.

High-order schemes are typically designed for accuracy and error reduction, with stability often ensured through spatial filtering rather than inherent stencil design. Existing multidimensional solid-wall treatments rely on ghost-point methods [17–21], yet their stability properties remain largely unexplored. Our recent formulation takes a different approach: instead of using ghost points outside the domain, we directly enforce boundary constraints while computing first derivatives near the boundary. These constraints are derived similarly to those proposed by Goodrich & Hagstrom [22] for wall-normal derivatives of pressure and velocity. Since acoustic flows are largely irrotational, we also incorporate a zero-vorticity condition [22] into the stencil design.

Although this approach produces highly accurate results, minor instabilities sometimes require additional stabilization. To address this, we demonstrate the stabilizing effect of radiation boundaries on the solid-wall treatment for exterior acoustical problems.

1.1 Goals and outline of the paper

So far, numerical stability assessments of immersed-boundary schemes have been limited to 1D. For multidimensional schemes, including our approach, no systematic investigations exist regarding potential numerical instabilities. To better understand how to control their extent, we aim to analyze the stability of solid-wall boundary schemes for the multidimensional LEE. Specifically, we seek to evaluate the stability properties of our multidimensional immersed-boundary method [16]. Since Tam's [15] truncated matrix method in 1D does not easily extend to multiple dimensions, we adopt the matrix method to study multidimensional problems.

The paper is structured as follows: Section 2 presents the governing equations - the linearized Euler equations (LEE) - along with the relevant solid-wall boundary conditions. Section 3 introduces our multidimensional cut-cell method, detailing its stencil design using a 2D cylinder as an example. Section 4 outlines the matrix method and its eigenvalue analysis for the multidimensional LEE, incorporating non-reflective boundary conditions. Section 5 examines eigenvalues of two boundary schemes to identify stable discretizations around a 2D cylinder, followed by aeroacoustic benchmarks: planar wave scattering and aeolian sound emission from low-Reynolds-number flow around a 2D cylinder. Finally, Section 6 summarizes key findings.

2. LINEARIZED EULER EQUATIONS (LEE)

The linearized Euler equations (LEE) in nondimensional form for the isentropic case with a uniform background flow [23] are given in index notation as

$$\frac{\partial v_i}{\partial t} + \mathrm{Ma}\, V_j \frac{\partial v_i}{\partial x_j} + \frac{\partial p}{\partial x_i} = 0\,, \tag{1a}$$

$$\frac{\partial p}{\partial t} + \mathrm{Ma}\, V_j \frac{\partial p}{\partial x_j} + \frac{\partial v_j}{\partial x_j} = 0\,, \tag{1b}$$

where v_i and p are the perturbed velocity components and pressure, normalized by the speed of sound c_0 and $\rho_0\, c_0^2$, respectively. Spatial and temporal variables x_i and t are normalized by a reference length L_0 and L_0/c_0. Here, the background velocity components V_i are scaled by a reference velocity V_0 (as used for the determination of a Reynolds number), leading to the Mach number $\mathrm{Ma} = V_0/c_0$ as an additional scaling parameter.

The LEE (1) describe transient, non-dispersive, and non-dissipative wave propagation of a fluid featuring a fixed nondimensional speed of sound equal to one. In the absence of background flow ($\mathrm{Ma} = 0$), the wave solutions satisfy an irrotational motion with vanishing vorticity.

2.1 Solid-Wall Boundary Conditions

When solid obstacles are present, wave scattering and reflection must also be accounted for. The fundamental physical boundary condition at a solid wall is the impermeability (free-slip) condition:

$$v_i\, n_i = 0\,, \tag{2}$$

which ensures that no fluid can penetrate the wall in its normal direction n_i.

Previously, we [16] derived an infinite set of multidimensional boundary constraint equations for arbitrary wall locations and orientations in M-dimensional space. These constraints are applied at so-called surface enforcement points (SEP) of the discretized solid wall, extending the work of Goodrich & Hagstrom [22]. By projecting the momentum balance equations (1a) on the wall-normal direction n_i, enforcing the impermeability condition (2), and repeating this process for the mass balance equation (1b), the infinite set of conditions

$$v_i\, n_i = 0\,, \quad \frac{\partial p}{\partial x_i} n_i = 0\,, \quad \frac{\partial^2 v_j}{\partial x_j\, \partial x_i} n_i = 0\,,$$
$$\frac{\partial^3 p}{\partial x_j^2\, \partial x_i} n_i = 0\,, \quad \frac{\partial^4 v_k}{\partial x_k\, \partial x_j^2\, \partial x_i} n_i = 0\,, \ldots \tag{3}$$

is obtained. These constraints hold at any nodal or internodal position as illustrated in Fig. 1. The second constraint in (3)

$$\frac{\partial p}{\partial x_i} n_i = 0\,, \tag{4}$$

represents the vanishing wall-normal pressure gradient, which supports the enforcement of the impermeability condition. When the wall is located on a grid node, conditions (2) and (4) are equivalent. This has led several authors [17, 18, 20] to rely solely on the pressure gradient condition for implementing solid walls. However, discretely enforcing the zero pressure gradient condition at an internodal position does not necessarily satisfy the impermeability condition at that same location. To improve accuracy, we always incorporate at least the first two physical boundary conditions (2) and (4) in our stencil design. The higher-order constraints are employed to enhance the numerical stability of the boundary discretization near solid walls.

When including a nonzero uniform background flow, the linearized Euler equations (LEE) (1) inherently contain perturbed vortical modes that are not damped due to their inviscid formulation. For nonuniform background flow, the solution of the LEE may become unstable and diverge when hydrodynamic instabilities arise [24]. In contrast, the LEE without background flow (Ma $= 0$) do not support the generation of perturbed vorticity [22], which is defined as the curl of the perturbed velocity v_k

$$\omega_i = \epsilon_{ijk} \frac{\partial v_k}{\partial x_j} = 0\,, \tag{5}$$

$$\text{or} \quad \omega_3 = \frac{\partial v_2}{\partial x_1} - \frac{\partial v_1}{\partial x_2} = 0 \quad \text{specifically in 2D}\,. \tag{6}$$

3. SPATIAL DISCRETIZATION APPROACH

We aim to solve the LEE (1) using finite-difference methods on Cartesian grids. Employing high-order explicit central stencils with optimized coefficients as in Tam & Webb (DRP) [23] or Bogey & Bailly [25] throughout the entire domain for approximating first-order spatial derivatives, as in eq. (7), ensures numerical stability and accuracy. However, the stability of such finite-difference methods is compromised when the consistent use of central stencils is disrupted - such as when biased stencils of the same order are employed near embedded obstacles or global domain boundaries. While reducing the stencil order at boundaries improves numerical stability, it also leads to a significant loss of accuracy [26].

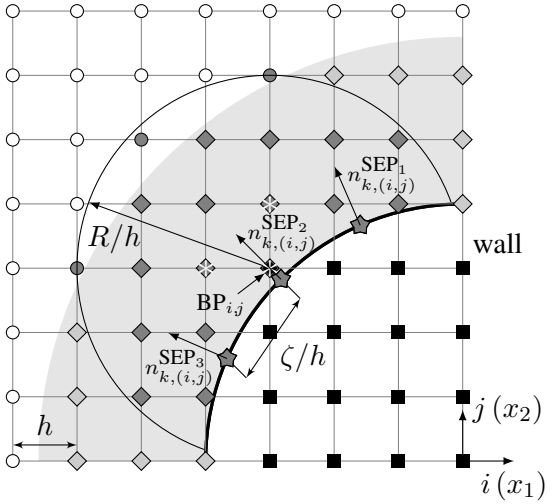

Figure 1: Sketch of the boundary discretization for modified stencils at boundary points for a quarter of a circular cylinder with a diameter of $8h$ when using a 7-point stencil in the domain's interior. ▒ boundary region, ○ point in fluid region (FP), ◇ point in boundary region (BP); every BP is a FP as well, ✩ surface enforcement point (SEP), ∗ volume enforcement point (VEP), ■ point in solid region.

To retain accuracy near boundaries, we previously introduced a consistent and stable immersed-boundary method that constructs modified discretizations near solid walls [16] by incorporating a tailored subset of boundary constraints (Fig. 1). This approach enables the stable solution of the linearized Euler equations in 1D without the need for spatial filters. We further demonstrated its applicability to higher dimensions through numerical cases involving wave scattering at arbitrarily immersed cylinders with various resolutions. However, in multidimensional settings, minor instabilities in the boundary discretization necessitated the use of modified filter schemes, applying the same principles as the modified derivative stencils.

In this study, we improve the stability of the boundary discretization to eliminate the need for spatial filtering. The following sections revisit the boundary-point method (BPM) introduced in [16] and demonstrate its application to the multidimensional LEE and LPCE, including cases with inhomogeneous background flow.

3.1 Multidimensional High-Accuracy Stencil Design Near Immersed Boundaries

We revisit the general procedure for designing Hermite-based finite-difference stencils that incorporate a known subset of boundary constraints derived from the LEE, as given in eqs. (3) and (5). The interaction of acoustic waves with solid obstacles involves multiple physical effects, such as reflection, refraction, and scattering. To minimize numerical discretization errors, we employ Cartesian grids with an equidistant, nondimensional grid spacing h near the boundary. From now on, we express spatial locations using nondimensional indices $i = x_1/h$ and $j = x_2/h$, where integer values indicate nodal positions and internodal positions are described by real-valued indices. We use standard central n'th-order finite-difference stencils, which involve $n+1$ nodes in the domain's interior and have a truncation error of $\mathcal{O}(h^n)$. For example, a seven-point stencil approximates the first derivative at an interior node i, j in 2D along the x_1-direction using the discretization operator d_1^ϕ:

$$\left.\frac{\partial \phi}{\partial x_1}\right|_{i,j} \equiv \frac{1}{h}\left. d_1^\phi \right|_{i,j} \approx \frac{1}{h}\sum_{m=-3}^{3} a_m \phi_{i+m,j} \qquad (7)$$

where the finite difference coefficients are $a_m = (-1/60, 3/20, -3/4, 0, 3/4, -3/20, 1/60)$. The symmetry of central stencils eliminates amplitude errors, while dispersive errors - associated with phase- and group-velocity inaccuracies - can be mitigated for a prescribed spectral range by reducing the stencil's order, as demonstrated in DRP (Dispersion-Relation-Preserving) schemes by Tam & Webb [23].

Consider a circular cylinder with diameter D immersed in a uniform 2D Cartesian grid with mesh width h, as depicted in Fig. 1. The nondimensional diameter, defined as PPD $= D/h$, is set to 8 PPD. We define a 'boundary region' extending approximately $n/2$ grid points perpendicularly from the obstacle into the domain. The set of all grid points within this shaded boundary region is referred to as *boundary points* (BP), where modifications to the discretization of the balance equations are required. Finite-difference approximations at all other grid points outside this boundary region remain unchanged and can be computed using the standard weighted sum in eq. (7).

The solid wall forms an arbitrary closed curve in 2D (or a closed surface in 3D), mostly meandering between the grid nodes i, j. Thus, we must discretize the boundary by representing it as a finite set of line segments (surface elements) connected by points, which we define as *surface enforcement points* (SEP). Each BP is associated with a specific set of SEPs, which are defined by their coordinates x_k^{SEP} and corresponding wall-normal directions n_k^{SEP}. Boundary conditions are enforced at these discrete SEPs. The stability of our immersed boundary method critically depends on selecting an appropriate SEP configuration for each BP. In Fig. 1, we illustrate an example where three SEPs are spaced approximately 1.5 grid points apart. The shortest nondimensional distance between these SEPs denoted ζ/h, plays a key role in constructing robust and accurate immersed-boundary schemes, as demonstrated through stability analyses and numerical tests in 2D.

Findings from the 1D immersed-boundary schemes [16] can be extended to multidimensional cases. In 1D, the number of boundary constraints determined the stability of the discretization. However, multidimensional boundary treatments are more complex. Nonetheless, incorporating a subset of the infinite set of multidimensional boundary constraints from eq. (3) is essential to maintain consistency with the 1D approach. While these constraints hold in the continuous analytical formulation, their discrete enforcement requires careful consideration. Instead of using ghost points, our approach integrates boundary constraints directly into the stencil formulation, similar to compact schemes (Lele [14]) or Hermitian finite-difference schemes (Goodrich [27]). Rather than computing derivatives, including ghost values, our stencils approximate derivatives while simultaneously enforcing the incorporated boundary constraints. In 1D, we demonstrated that our approach is mathematically equivalent to ghost-point formulations in certain cases, precisely when the number of constraints matches the number of unique ghost points. However, in multidimensional settings, the number of usable ghost points in convex regions of the surface enclosing an obstacle is limited, making our approach more rigorous.

We start with a general 2D Taylor series expansion for an arbitrary r'th-order derivative of a variable ϕ about a node i, j along the x_q- and x_p-directions

$$\begin{aligned}\left.\frac{\partial^r \phi}{\partial x_q^s \partial x_p^{r-s}}\right|_{m,n} &= \left.\frac{\partial^r \phi}{\partial x_q^s \partial x_p^{r-s}}\right|_{i,j} \\ &+ \frac{h}{1!}\left.\frac{\partial^{r+1}\phi}{\partial x_q^s \partial x_p^{r-s}\partial x_k}\right|_{i,j}\frac{\Delta x_k}{h} \\ &+ \frac{h^2}{2!}\left.\frac{\partial^{r+2}\phi}{\partial x_q^s \partial x_p^{r-s}\partial x_k \partial x_l}\right|_{i,j}\frac{\Delta x_k}{h}\frac{\Delta x_l}{h} + \cdots \qquad (8)\end{aligned}$$

where $\Delta x_1/h = m - i$ and $\Delta x_2/h = n - j$, and the side constraint $s \leq r$ applies. Extending the formulation to 3D requires analogous Taylor series expansions in 3D.

A discrete Hermite-based function approximation can be constructed using a weighted linear combination of d arbitrary r'th-order derivatives (8) reading

$$\alpha_d \left(h^r \left. \frac{\partial^r \phi}{\partial x_q^s \partial x_p^{r-s}} \right|_{m,n} \right)_d \approx 0\,. \tag{9}$$

The coefficients α_d ensure that the stencil preserves Taylor-series correlations up to a desired order of h. For $r = 0$, expression (9) includes the (known) nodal values, whereas one or several first derivatives ($r = 1$) are the unknowns to be approximated. This formulation allows us to enforce boundary conditions naturally within the finite-difference framework, leading to accurate and stable numerical schemes.

To demonstrate the practical application of the previous derivations, consider the explicit approximation of the perturbation pressure gradient $\partial p/\partial x_i$ at a boundary point denoted as $\mathrm{BP}_{i,j}$. Our goal is to extend the seven-point central discretization from the interior while maintaining accuracy near the boundary. By defining a circular subset of 19 fluid points (FPs) with a nondimensional radius $R/h = 3$, we formulate an approximation for the first derivative $\partial p/\partial x_1$ (weighted for convenience by $\alpha_0 = -1$), using the Hermitian ansatz

$$h \left. \frac{\partial p}{\partial x_1} \right|_{\mathrm{BP}_{i,j}} \approx \sum_{d=1}^{19} \alpha_d \, p|_{\mathrm{FP}_d}\,. \tag{10}$$

To incorporate boundary conditions into our stencil formulation, three surface-enforcement points (SEPs) are introduced on the boundary (ref. Fig. 1). There, the first-order boundary constraint $\partial p/\partial x_i \, n_i = 0$ is enforced, yielding

$$\left. \frac{\partial p}{\partial x_1} \right|_{\mathrm{BP}_{i,j}} \approx \frac{1}{h} \sum_{d=1}^{19} \alpha_d \, p|_{\mathrm{FP}_d} + \sum_{d=20}^{22} \alpha_d \left. \frac{\partial p}{\partial x_i} n_i \right|_{\mathrm{SEP}_{d-19}}\,. \tag{11}$$

Further constraint equations from eq. (3) can be included straightforwardly.

In this example, the final stencil's dimension is 22, requiring a linear system of equations to determine α_d. Given the Taylor-series expansion constraints, e.g., for 6th-order accuracy, 28 terms need to be satisfied, an overdetermined linear system of equations structured as $A_{cd}\,\alpha_d = b_c$ can be formulated. Here, A_{cd} is a non-square 28×22 matrix, α_d is the 22×1 coefficient vector, and b_c is a 28×1 right-hand side vector.

It turns out that singular value decomposition (SVD) is a suitable approach for finding an approximative solution, ensuring condition numbers $\leq 10^8$. The resulting coefficients α_d, determining the modified pressure derivative at the $\mathrm{BP}_{i,j}$, optimize stability and accuracy. The method is efficiently implemented when the coefficients α_d are computed once in a preprocessing step and stored for repeated usage during the time-stepping procedure.

For vectorial equations such as the momentum balance (1a), boundary conditions like the free-slip condition $v_i \, n_i = 0$ must be incorporated into the velocity stencils requiring analogous coupled formulations for the velocity components. Further modification and improvement are achieved by enforcing zero vorticity at SEPs or additional VEPs.

4. MULTIDIMENSIONAL STABILITY ANALYSIS VIA THE MATRIX METHOD

The stability of discretized multidimensional linearized Euler equations (LEE) is crucial for obtaining convergent numerical solutions in aeroacoustics. Here, we consider the nondimensional LEE with zero mean flow (Ma = 0). We assess the stability of the proposed immersed boundary formulation using the matrix method [6], which involves analyzing the eigenvalues of the discretized system. Given the complexity of multidimensional boundary conditions, we do not attempt a general proof of stability but instead identify key parameters influencing stability.

A Cartesian grid in 2D space including $M_1 \times M_2 = M$ nodes is considered. Since acoustic waves radiate outward at the global boundaries non-reflective boundary conditions are applied. Traditional methods include characteristic boundary conditions [28], perfectly matched layers (PML) [29], and sponge zones (buffer layers) [30]. Here, we focus on sponge zones that modify the governing equations within a specific region and, thus, damp the numerical solution before reaching the global boundary.

Following Israeli and Orszag [30], we introduce a damping term in the transport equation, e.g., $\partial p/\partial t + \partial v_i/\partial x_i = -\kappa/h\,(p - p_0)$ where κ is a spatially varying damping factor, commonly defined as $\kappa(x/h) = \kappa_0(1 - x/(h\,N_{\mathrm{buffer}}))^\beta$ and p_0 is an arbitrary target value. Here, κ_0 is the maximum damping amplitude, β controls the

damping profile, and N_{buffer} is the number of buffer zone nodes. The central stencil width is successively reduced towards the global boundary.

Using the method-of-lines (MOL) [7], we discretize spatial derivatives while keeping time continuous to focus on spatial discretization effects. Applying a nodal time-harmonic ansatz $\phi_l(t) = \hat{\phi}_l \exp(-i\,\tilde{\omega}\,t)$ to the semi-discretized LEE leads to the frequency-space form

$$[(\kappa - i\omega)\ \hat{v}_k + d_k^p \hat{p}]_l = 0\,, \tag{12a}$$
$$[(\kappa - i\omega)\ \hat{p} + d_k^{v_k} \hat{v}_k]_l = 0\,. \tag{12b}$$

for every node $l = 1, \ldots, M$ with the abbreviated eigenvalue $\omega = \tilde{\omega}\,h$. In eq. (12), the index $k = 1, 2$ in 2D and d_k^ϕ denotes the discretization operator introduced in eq. (7) respectively its modifications at boundary points.

The unknown amplitudes for the pressure $\hat{p}$ and the velocity components $\hat{v}_i$ are arranged into a $3M$-dimensional vector $V_k \equiv (\hat{p}_M\ \hat{v}_{1,M}\ \hat{v}_{2,M})$. This results in the eigenvalue problem

$$\underbrace{(\omega\,\delta_{mk} - D_{mk})}_{=A_{mk}(\omega)} V_k = 0\,, \tag{13}$$

with the identity matrix represented by the Kronecker delta δ_{mk} and the $3M \times 3M$ discretization matrix

$$D_{mk} = -i \begin{bmatrix} \kappa|_l & d_1^{v_1}|_l & d_2^{v_2}|_l \\ d_1^p|_l & \kappa|_l & 0 \\ d_2^p|_l & 0 & \kappa|_l \end{bmatrix} \tag{14}$$

comprising $M \times M$ submatrices for spatial derivatives $d_i^\phi|_l$, including the modified boundary stencils and nonzero damping terms $\kappa|_l$ along the diagonal. Since our scheme avoids ghost points, boundary coefficients like interior stencils are directly integrated into the matrix. Oblique cut-cell boundaries increase the matrix density due to the coupling of velocity components via the impermeability condition (2) at SEPs and the zero-vorticity constraint (6) at SEPs and VEPs.

Solving for the eigenvalues ω from $\det(A_{mk}(\omega)) = 0$ yields the stability condition - the spatial discretization is unconditionally stable if $\Im\{\omega\} \leq 0$ for all eigenvalues.

5. COMPUTATIONAL RESULTS

We demonstrate the application of the stability analysis tool (Section 4) to optimize boundary stencil parameters. As a test case, a circular cylinder immersed in a regular Cartesian grid is analyzed, assessing the spatial discretization for the LEE. Further, we apply our computational schemes to two benchmark problems. First, the scattering of a planar wave at the embedded cylinder and secondly, the flow-induced noise from a low-Reynolds flow around the cylinder, solving the LPCE from Seo & Moon [31] without applying any spatial filtering techniques. These cases highlight two key aspects: (1) our immersed boundary scheme yields high accuracy, and (2) our stability analysis, formulated for the LEE without background flow, reliably assesses the stability, avoiding the necessity of using spatial filters.

5.1 Investigating the stability

We analyze the stability of a circular cylinder with a diameter $8h$ by setting up a 48×48 computational domain with an equidistant mesh width $h = 1$. The cylinder's midpoint location is varied around the domain center as $x_i/h + \eta_i = (24 + \eta_1, 24 + \eta_2)$ in order to generate a variety of cut-cell configurations. The boundary stencils modify the discretization at 96 surrounding BPs for $\eta_i = 0$ (ref. Fig. 1) and $\eta_i = (0.5\,, 0.5)$ respectively, and at 92 BPs for $\eta_i = (0.99\,, 0.99)$. The nondimensional radius of the stencil formulation is $R/h = 3$, i.e., nodes within this radius around each BP (but still in the fluid region) contribute to the first-order derivative computations. To enforce non-reflective boundary conditions, sponge zones extend five nodes ($N_{\text{buffer}} = 5$) into the domain from each global boundary. The damping parameters are set to $\kappa_0 = 1$ and $\beta = 3$, with homogeneous target values $p_0 = v_{i,0} = 0$.

Due to space limitations, an extensive survey of boundary formulations is not feasible, so only two configurations are investigated. The first and most straightforward approach incorporates a single enforcement point (SEP) per BP. The SEP is determined as the intersection of a straight line connecting the BP to the cylinder's midpoint with the cylinder's surface. At this SEP, only the impermeability condition (2) and the vanishing wall-normal pressure gradient (4) are discretely enforced. This boundary scheme is referred to as 'bs1'.

The second configuration, denoted as 'bs2', introduces three SEPs per BP, as illustrated in Fig. 1. The middle SEP is determined as in 'bs1', while the neighboring SEPs are positioned by rotating the middle SEP approximately $\pm 21.5°$ around the cylinder's midpoint. In this case, the first three constraint equations from (3) are en-

forced for v_i and p. Additionally, the zero-vorticity constraint (6) is applied at all SEPs. The enforcement of the zero-vorticity condition $\omega_3 = 0$ at VEPs depends on the displacement vector η_i. For $\eta_i = 0$, the condition is enforced at non-diagonally located fluid points (FPs) within a radius $R/h \leq 1$. When $\eta_i = (0.5\,, 0.5)$, $\omega_3 = 0$ is only enforced at the BP itself. Finally, for $\eta_i = (0.99\,, 0.99)$, no vorticity enforcement is applied at VEPs.

Fig. 2 presents the eigenvalue distributions for the two boundary schemes under investigation. The simple scheme 'bs1' (Fig. 2a) exhibits a cluster of highly unstable eigenvalues positioned on the imaginary axis ($\Re\{\omega\} = 0$), with magnitudes reaching the order of one. Given that the damping magnitude κ_0 at the global boundaries is of the same order, the numerical solution experiences significant amplification due to boundary instabilities from the boundary discretization. Nevertheless, apart from these unstable modes, the majority of eigenvalues reside in the stable negative complex half-plane. As a result, the buffer layers effectively damp most eigenmodes over time.

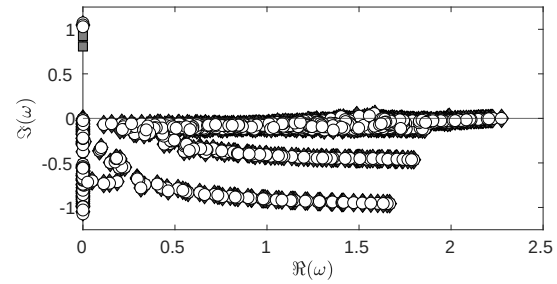

(a) 'bs1'

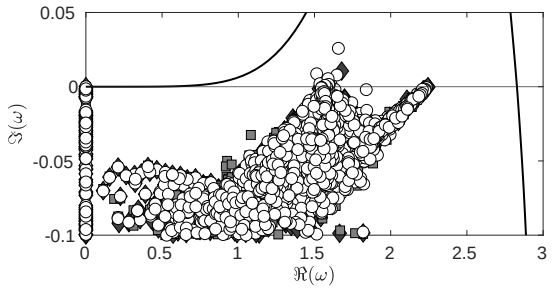

(b) 'bs2'

— stability region of the RK4 time-integrator.

Figure 2: Normalized eigenvalue spectra ω of the discretized LEE in 2D using 7-point central stencils in the domain's interior and modified boundary stencils' bs1' and 'bs2' near the circular cylinder with 8 PPD including buffer-layers. ◆, $\eta_i = 0$, ■ $\eta_i = (0.5\,, 0.5)$, ○ $\eta_i = (0.99\,, 0.99)$.

In contrast, the optimized boundary scheme 'bs2' (Fig. 2b) eliminates the prominent unstable eigenvalues previously observed on the imaginary axis. However, depending on the displacement vector η_i, still minor instabilities can emerge, with magnitudes two orders smaller than those in 'bs1', occurring around $\Re\{\omega\} \approx 1.6$. When $\eta_i = (0.5\,, 0.5)$, all eigenvalues satisfy $\Im\{\omega\} < 0$, ensuring that the spatial discretization scheme remains asymptotically stable. For other configurations, the 4th-order Runge Kutta time-integration scheme can provide sufficient damping for these minor instabilities, given an appropriately chosen CFL number. Specifically, all eigenvalues remain within the stability region of the RK4 time integrator for CFL=1 in Fig. 2b, ensuring numerical stability.

Consequently, spatial filtering techniques are unnecessary in this case. However, decreasing the CFL number for accuracy improvements may shift some unstable eigenvalues outside the stability region of the time integrator. Therefore, the interaction between temporal and spatial discretization requires careful consideration to maintain stability while optimizing accuracy.

5.2 Scattering of a planar wave

The scattering of a planar wave resolved by 8 PPW at the circular cylinder from the previous subsection is investigated. For that, a 128×128 computational domain is considered where the circular cylinder is located at $x_i/h + \eta_i = (64.99, 64.99)$ in order to demonstrate the high acccuracy of the boundary formulation 'bs2'. The solution is advanced in time using a fourth-order Runge-Kutta scheme (RK4) with a nondimensional timestep of CFL = 2/3. To minimize reflections at the global boundaries, we employ non-reflective sponge zones, extending 16 nodes into the computational domain. The damping parameters are $\kappa_0 = 1$ and $\beta = 3$.

Fig. 3 presents the pressure solution along the diagonal $x_2 = x_1$. The numerical solution exhibits minimal deviation from the exact solution [33], demonstrating the high accuracy of the boundary treatment. Furthermore, for the chosen CFL number, the investigated boundary scheme 'bs2' remains stable without requiring spatial filtering. Similar results can be obtained for the other cut-cell configurations examined in Section 5.1.

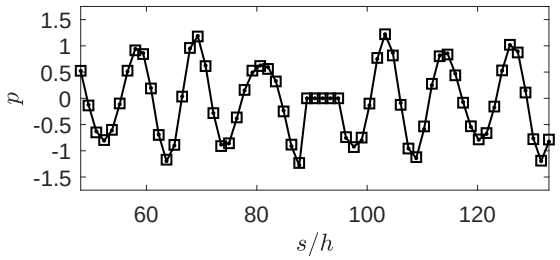

Figure 3: Normalized pressure of a scattered planar wave (8 PPW) at a cylinder ($\eta_i = (0.99\,, 0.99)$) evaluated along the diagonal line $x_2 = x_1$ for the boundary scheme 'bs2' and an optimized central 7-point scheme (Richter [32]) in the interior of the domain and CFL = 2/3. —•— exact, □ 'numerical'.

5.3 Flow-induced noise from a low-Reynolds flow past a circular cylinder

We present numerical results for the classical aeroacoustic problem of flow-induced tonal noise generated by a low-Reynolds-number flow past a circular 2D cylinder using the LPCE of Seo & Moon [31]. We consider a Reynolds number Re $= 150$ and a Mach number Ma $= 0.2$. The incompressible CFD solution is computed using a pressure-based solver in Ansys® Fluent, 2024 R1 with a second-order implicit time integration scheme on a structured O-grid ($400D \times 400D$, $\Delta x_{\text{min}}/D \approx 0.005$), totaling 309,000 quadrilateral elements. Time integration uses a nondimensional timestep of $\tau_{\text{CFD}} = \Delta t_{\text{CFD}} V_0/D = 0.05$, covering one vortex shedding cycle in 109 steps. Using the coupled solver, 25 inner iterations are required to drive the residual for continuity below 10^{-9}. The nondimensional vortex shedding frequency is given by the Strouhal number $\text{St}_l \approx 0.183$, with a second harmonic at $\text{St}_d \approx 0.366$, corresponding to the drag dipole. The nondimensional wavelengths of the lift dipole are $\lambda_l/D = 1/(\text{St}_l\,\text{Ma}) \approx 27.3$, and for the drag dipole, Doppler-corrected values range from $\lambda_d/D \approx 10.9$ upstream to 16.4 downstream for Ma $= 0.2$. Sponge zones [30] are used as non-reflective boundary treatments with a length of $L_{\text{buffer}} \approx 2\lambda_l/D$.

For the LPCE discretization, the cylinder is resolved by 8 points per diameter (PPD) in an equidistant $5D \times 5D$ square (40×40 lattice), yielding sufficient accuracy for wave propagation and scattering with a classical seven-point DRP scheme, as demonstrated before. Beyond this, the acoustic grid expands to $400D \times 400D$, forming a structured 400×400 layout with 160,000 nodes. The minimal mesh width $h/D = 1/\text{PPD} = 0.125$ of the CAA grid is 25 times larger than the minimal mesh width of the CFD grid. Using an RK4 scheme with a CFL number of one results in a nondimensional CAA timestep $\tau_{\text{CAA}} = \text{CFL}/\text{PPD} = 0.125$, which is half the Mach number scaled CFD timestep $\tau^*_{\text{CFD}} = \tau_{\text{CFD}}/\text{Ma} = 0.25$. Consequently, the CFD source term DP/Dt from the incompressible CFD solution has not been interpolated in time, considering its sufficient temporal resolution of 109 points per period. Instead, compact radial basis functions [34] project the CFD-source data onto the acoustic grid using Wendland's C-2 kernel [35] with 15 points per interpolator.

In the LPCE approach, instantaneous acoustic pressure perturbations are computed as $\Delta p' = P + p' - \overline{P + p'}$ at each timestep, where P is the hydrodynamic pressure from the CFD solution, p' is the perturbed pressure from the LPCE and $\overline{P + p'}$ represents the time-averaged pressure field over a complete shedding cycle here. The RMS-pressure fluctuations $\Delta p'_{\text{RMS}}$ shown in Fig. 4 confirm dominant dipole sound emission and minor drag dipole effects, with comparisons to a DNS by Inoue & Hatakeyama [36] validating the accuracy of the immersed boundary implementation for a case with inhomogeneous background flow. The use of a coarse equidistant Cartesian grid with boundary treatment near the cylinder enables large timesteps for the CAA solution without requiring spatial filters or sacrificing accuracy.

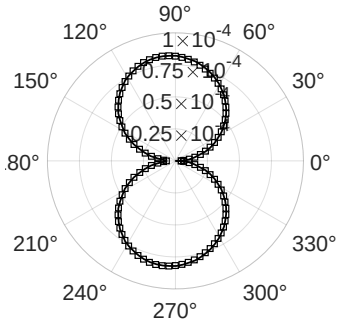

Figure 4: Polar plot of $\Delta p'_{\text{RMS}}$ at $r/h = 75$ for Re $= 150$ and Ma $= 0.2$. The cylinder's diameter $D/h = 8$. The boundary scheme 'bs2' ($\eta_i = (0.5\,, 0.5)$) and an optimized central 7-point scheme (Richter [32]) in the interior of the domain is used. CFL = 1. —— exact (DNS from Inoue & Hatakeyama [36]), □ 'numerical'.

6. CONCLUSIVE REMARKS

This paper presents a stability analysis and computational validation of an immersed boundary scheme for solving the LEE/LPCE in aeroacoustics. The stability of the discretized equations is assessed using the matrix method, where eigenvalue decomposition helps determine whether the numerical scheme remains stable. Sponge zones are used as non-reflective boundary treatments to handle wave radiation at the global boundaries. Two boundary schemes are tested: the simpler 'bs1' scheme, which exhibits significant instability, and the refined 'bs2' scheme, which successfully suppresses most unstable eigenvalues and ensures better stability by incorporating a considerate set of constraint equations, including a zero-vorticity condition.

The computational validation involves two test cases. First, the scattering of a planar wave resolved with 8 points per wavelength by a circular cylinder is simulated, showing excellent agreement with analytical solutions and confirming the accuracy of the boundary treatment. Second, flow-induced noise from a low-Reynolds-number flow ($\mathrm{Re} = 150, \mathrm{Ma} = 0.2$) around a circular cylinder is investigated using the LPCE. The numerical results align well with DNS reference data, demonstrating that the immersed boundary method enables stable simulations, including nonhomogeneous background flow, without the need for spatial filtering.

Overall, the study confirms that the proposed boundary scheme provides both stability and accuracy at affordable computational cost, making it suitable for aeroacoustic applications involving complex geometries and immersed boundaries.

7. REFERENCES

[1] R. Courant, K. Friedrichs, and H. Lewy, "Über die partiellen Differenzengleichungen der mathematischen Physik," *Mathematische Annalen*, vol. 100, pp. 32–74, Jan. 1928.

[2] P. D. Lax and R. D. Richtmyer, "Survey of the stability of linear finite difference equations," *Communications on Pure and Applied Mathematics*, vol. 9, no. 2, pp. 267–293, 1956.

[3] J. G. Charney, R. Fjörtoft, and J. von Neumann, "Numerical integration of the barotropic vorticity equation," *Tellus A: Dynamic Meteorology and Oceanography*, Jan. 1950.

[4] R. Vichnevetsky and J. B. Bowles, *Fourier Analysis of Numerical Approximations of Hyperbolic Equations*. Society for Industrial and Applied Mathematics, 1982.

[5] B. Gustafsson, H.-O. Kreiss, and A. Sundström, "Stability theory of difference approximations for mixed initial boundary value problems. ii," *Mathematics of Computation*, vol. 26, no. 119, pp. 649–686, 1972.

[6] C. Hirsch, *Numerical computation of internal and external flows. Vol. 2 - Computational methods for inviscid and viscous flows*. Wiley, New York, 1990.

[7] 0. A. Liskovets, "The method of lines (review)," in *Differential Equations 1*, pp. 308–1323, 1965.

[8] M. N. Mikhail, "On the validity and stability of the method of lines for the solution of partial differential equations," *Applied Mathematics and Computation*, vol. 22, no. 2, pp. 89–98, 1987.

[9] D. Jones, J. South, and E. Klunker, "On the numerical solution of elliptic partial differential equations by the method of lines," *Journal of Computational Physics*, vol. 9, no. 3, pp. 496–527, 1972.

[10] H.-O. Kreiss, "Über die Stabilitätsdefinition für Differenzengleichungen die partielle Differentialgleichungen approximieren," *BIT*, vol. 2, p. 153–181, Sep. 1962.

[11] S. Osher, "Systems of difference equations with general homogeneous boundary conditions," *Transactions of the American Mathematical Society*, vol. 137, pp. 177–201, 1969.

[12] J. C. Strikwerda, "Initial boundary value problems for the method of lines," *Journal of Computational Physics*, vol. 34, no. 1, pp. 94–107, 1980.

[13] A. Sescu, R. Hixon, C. Sescu, and A. Afjeh, "Stability investigation of multidimensional optimized spatial stencils," *AIAA 2009-5. 47th AIAA Aerospace Sciences Meeting including The New Horizons Forum and Aerospace Exposition*, 2009.

[14] S. K. Lele, "Compact finite difference schemes with spectral-like resolution," *Journal of Computational Physics*, vol. 103, no. 1, pp. 16–42, 1992.

[15] C. K. W. Tam and K. A. Kurbatskii, "A wavenumber based extrapolation and interpolation method for use in conjunction with high-order finite difference schemes," *Journal of Computational Physics*, vol. 157, no. 2, pp. 588–617, 2000.

[16] M. G. S. Izsak and H.-J. Kaltenbach, "Improvement of the stability and accuracy of solid-wall immersed boundary schemes for the linearized Euler equations using boundary constraints," *Journal of Computational Physics*, vol. 473, p. 111728, 2023.

[17] K. A. Kurbatskii and C. K. W. Tam, "Cartesian boundary treatment of curved walls for high-order computational aeroacoustics schemes," *AIAA Journal*, vol. 35, no. 1, pp. 133–140, 1997.

[18] J. H. Seo and R. Mittal, "A high-order immersed boundary method for acoustic wave scattering and low-Mach number flow-induced sound in complex geometries," *Journal of Computational Physics*, vol. 230, no. 4, pp. 1000–1019, 2011.

[19] Y. Fukushima, T. Misaka, S. Obayashi, D. Sasaki, and K. Nakahashi, "Wavenumber optimized immersed boundary method for aeroacoustic analysis based on Cartesian mesh," *AIAA Journal*, vol. 54, no. 10, pp. 2988–3001, 2016.

[20] M. Cand, *A 3D High-Order Aeroacoustics Model for Turbomachinery Fan Noise Propagation*. PhD thesis, Imperial College London, 2005.

[21] I. Spisso and A. Rona, "Towards a monotonicity-preserving inviscid wall boundary condition for aeroacoustics," *AIAA 2009-3179. 15th AIAA/CEAS Aeroacoustics Conference (30th AIAA Aeroacoustics Conference)*, May 2009.

[22] J. Goodrich and T. Hagstrom, "High order implementations of accurate boundary conditions," *AIAA 1999-1942. 5th AIAA/CEAS Aeroacoustics Conference and Exhibit*, May 1999.

[23] C. K.W. Tam and J. C. Webb, "Dispersion-relation-preserving finite difference schemes for computational acoustics," *Journal of Computational Physics*, vol. 107, no. 2, pp. 262–281, 1993.

[24] R. Ewert and W. Schröder, "Acoustic perturbation equations based on flow decomposition via source filtering," *Journal of Computational Physics*, vol. 188, no. 2, pp. 365–398, 2003.

[25] C. Bogey and C. Bailly, "A family of low dispersive and low dissipative explicit schemes for flow and noise computations," *Journal of Computational Physics*, vol. 194, no. 1, pp. 194–214, 2004.

[26] M. G. S. Izsak and H.-J. Kaltenbach, "Improvement of high-order finite-difference schemes at solid walls for the linearized Euler equations," *AIAA 2022-2922. 28th AIAA/CEAS Aeroacoustics 2022 Conference*, Jun. 2022.

[27] J. Goodrich, T. Hagstrom, and J. Lorenz, "Hermite methods for hyperbolic initial-boundary value problems," *Mathematics of Computation*, vol. 75, no. 254, pp. 595–630, 2006.

[28] K. W. Thompson, "Time dependent boundary conditions for hyperbolic systems," *Journal of Computational Physics*, vol. 68, no. 1, pp. 1–24, 1987.

[29] J.-P. Berenger, "A perfectly matched layer for the absorption of electromagnetic waves," *Journal of Computational Physics*, vol. 114, no. 2, pp. 185–200, 1994.

[30] M. Israeli and S. A. Orszag, "Approximation of radiation boundary conditions," *Journal of Computational Physics*, vol. 41, no. 1, pp. 115–135, 1981.

[31] J. H. Seo and Y. J. Moon, "Linearized perturbed compressible equations for low Mach number aeroacoustics," *Journal of Computational Physics*, vol. 218, no. 2, pp. 702–719, 2006.

[32] C. Richter, *Liner Impedance modeling in the time domain with flow*. PhD thesis, Technische Universität Berlin, 2009.

[33] P. M. Morse and K. Uno Ingard, *Theoretical Acoustics*. International Series in Pure and Applied Physics. Princeton University Press, Princeton, 1968.

[34] D. Lazzaro and L. B. Montefusco, "Radial basis functions for the multivariate interpolation of large scattered data sets," *Journal of Computational and Applied Mathematics*, vol. 140, no. 1, pp. 521–536, 2002. Int. Congress on Computational and Applied Mathematics 2000.

[35] H. Wendland, "Piecewise polynomial, positive definite and compactly supported radial functions of minimal degree," *Advances in Computational Mathematics*, vol. 4, pp. 389–396, 1995.

[36] O. Inoue and N. Hatakeyama, "Sound generation by a two-dimensional circular cylinder in a uniform flow," *Journal of Fluid Mechanics*, vol. 471, p. 285–314, 2002.